Van der Waals Epitaxy and Photoresponse of Hexagonal Tellurium Nanoplates on Flexible Mica Sheets

Qisheng Wang,[†] Muhammad Safdar,[†] Kai Xu, Misbah Mirza, Zhenxing Wang, and Jun He*

National Center for Nanoscience and Technology, Beijing 100190, China. [†]Q. Wang and M. Safdar contributed equally.

ABSTRACT Van der Waals epitaxy (vdWE) is of great interest due to its extensive applications in the synthesis of ultrathin two-dimensional (2D) layered materials. However, vdWE of nonlayered functional materials is still not very well documented. Here, although tellurium has a strong tendency to grow into one-dimensional nanoarchitecture due to its chain-like structure, we successfully realize 2D hexagonal tellurium nanoplates on flexible mica sheets *via* vdWE. Chemically inert mica surface is found to be crucial for the lateral growth of hexagonal tellurium nanoplates since it (1) facilitates the migration of tellurium adatoms along mica surface and (2) allows a large lattice mismatch. Furthermore, 2D tellurium hexagonal nanoplates-based photodetectors are *in situ* fabricated on flexible mica sheets. Efficient photoresponse is obtained even after bending the device for 100 times, indicating 2D tellurium hexagonal nanoplates-based photodetectors on mica sheets have a great application potential in flexible and wearable optoelectronic devices. We believe the fundamental understanding of vdWE effect on the growth of 2D tellurium hexagonal nanoplate can pave the way toward leveraging vdWE as a useful channel to realize the 2D geometry of other nonlayered materials.

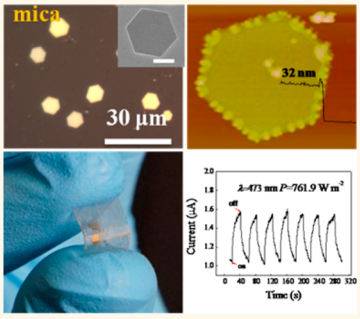

KEYWORDS: van der Waals epitaxy · 2D tellurium nanoplate · mica substrate · flexible device · photodetector

Van der Waals epitaxy (vdWE) has recently been identified as a facile synthesis technique in the growth of ultrathin two-dimensional (2D) layered materials[1−3] and their vertical heterostructures.[4,5] Unlike conventional heteroepitaxy, vdWE utilizes substrates whose surface is chemically inert because of the absence of surface dangling bonds such as fluorophlogopite mica.[6,7] In the vdWE growth, the overlayer and substrate are mainly connected by weak van der Waals interaction instead of strong chemical bonding.[8] Therefore, vdWE can circumvent strict requirement of lattice matching, enabling the growth of defect-free overlayer with different crystalline symmetry to that of substrate. In addition, vdWE allows overlayer to be perfectly relaxed without excessive strain in the heterointerface. These superior properties of vdWE make it a powerful technique to grow various 2D layered materials with highly single crystalline. As mentioned initially, vdWE has been successfully applied to prepare layered topological insulator Bi_2X_3 (X = Se or Te) nanoplates on mica,[7] graphene flakes on h-BN[9] or mica,[10] atomically thin III−VI semiconductor flakes on mica[3,11] and transition-metal dichalcogenide nanoplates on graphene[12] or mica.[1,13] Meanwhile, some researchers have dedicated their efforts to the vdWE growth of nonlayered materials such as ZnSe quantum dots on GaSe,[14] ZnO nanowire arrays on graphene,[15] InAs nanowires array on graphene[16] and GaAs nanowires array on graphene.[17] Very recently, Q. Xiong *et al.* further conducted the incommensurate vdWE growth of vertically aligned ZnO nanowires array[18] and II−VI tripod nanocrystals[19] on mica. These works are a big breakthrough in the development of vdWE since they extend the utilization of vdWE to the growth of nonplanar/nonlamellar nanoarchitectures. However, the utilization and characteristics of vdWE on 2D nanoarchitectures for many important nonlayered materials are still not very well documented. Furthermore, 2D nanoarchitectures are of great importance in fabricating electronic and optoelectronic device due to their compatibility with traditional microfabrication techniques. A fundamental research of vdWE effects on the growth of planar/lamellar nanoarchitectures of nonlayered materials

* Address correspondence to hej@nanoctr.cn.

Received for review May 23, 2014 and accepted July 2, 2014.

Published online July 02, 2014
10.1021/nn5028104

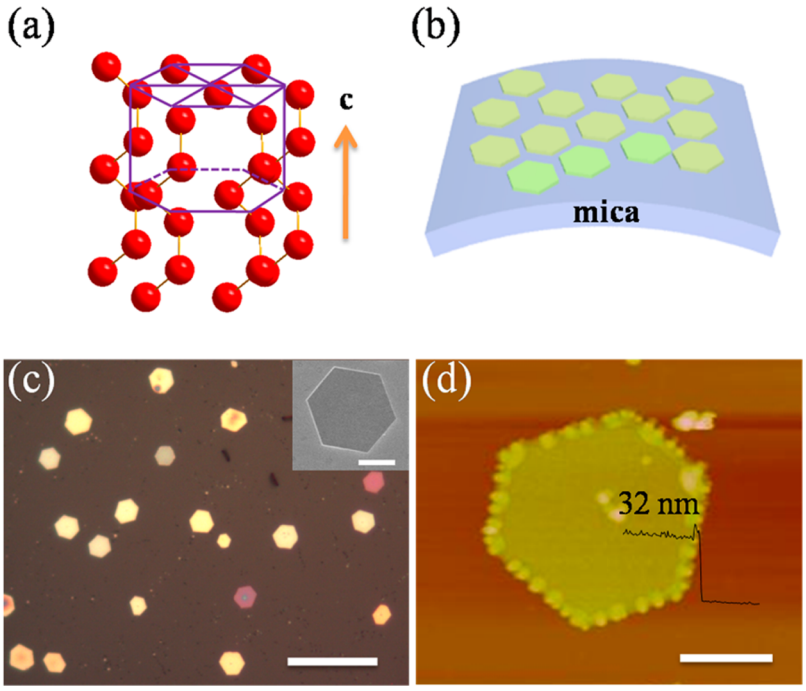

Figure 1. (a) Helical chain-like crystal structure of Se/Te. (b) Schematic illustration of 2D Te hexagonal nanoplates on flexible and transparent mica substrates by vdWE. (c) Typical OM image of 2D Te hexagonal nanoplates with scale bar of 30 μm. Inset: SEM image of single 2D Te hexagonal nanoplate, scale bar = 4 μm. (d) AFM image of a Te hexagonal nanoplate with thickness of 32 nm, Scale bar = 2 μm.

could enable the development of various functional devices such as flexible photodetector being discussed in this work.

Chalcogens, more specially, selenium (Se) and tellurium (Te) are p-type narrow band gap elemental semiconductors (1.6 eV for Se[20] and 0.34 eV for Te[21]). Chalcogens crystals have a highly anisotropic crystal structure as presented in Figure 1(a). Se or Te atoms first form the helical chains along *c*-axis by the covalent bonding. Then helical chains can be readily packed into a hexagonal crystal structure through van der Waals interactions. They are of great interest for their fascinating physical and chemical properties[22−26] such as high photoconductivity, anisotropy of the thermoconductivity, hydration and oxidation catalytic activity, high piezoelectric, thermoelectric and nonlinear optical responses. So far, a large number of one-dimensional (1D) chalcogens nanostructures have been achieved by a variety of synthesis methods such as microwave-assisted synthesis in ionic liquids,[27] vapor phase growth[28] and solution phase approach.[29] More importantly, chalcogens have a high reactivity toward a number of chemicals. Hence, chalcogens nanowires are usually used as the templates to generate a wealth of functional nanomaterials such as CdSe nanotubes,[30] PbTe nanowire,[31] Bi_2Te_3 nanowires,[32] Te nanowire-Bi_2Te_3 nanosheets heterostructure[33] and Te nanowire-In_2Te_3 nanosheets heterostructure.[34] However, to the best of our knowledge, few work reports the synthesis of 2D chalcogens nanoarchitectures, which is likely because chalcogens have a strong tendency to become 1D nanostructures due to its special crystal structure.

Recent study of substrate mediation in vapor deposition growth of $SnSe_2$ nanoplates revealed the migration barrier energy of $SnSe_2$ atoms on mica substrate is smaller than that on silicon (Si) substrate due to the absence of surface dangling bonds on mica substrate.[35] Furthermore, our previous work indicated that high-density Te pyramids with irregular hexagonal base were first assembled on the silicon (Si) surface before the growth of well aligned 1D Te arrays in the physical vapor deposition (PVD) process.[21] This feature is likely the result of strong interaction between Si substrate and Te atoms caused by the dangling bonds on Si surface, and the stacking of Te atoms along vertical direction. Thus, it is strongly expected to design the 2D regular hexagonal Te nanoplates *via* applying vdWE growth on mica sheets by PVD. Since mica provides a completely passivated surface that can interact with Te atoms through weak van der Waals forces. Consequently, high migration rate of Te adatoms on mica surface may lead to the faster growth of 2D Te nanoplates along the lateral direction.

Here we first demonstrate the vapor phase deposition of 2D hexagonal Te nanoplates on the flexible and transparent fluorophlogopite mica sheets *via* vdWE. The obtained 2D hexagonal Te nanoplate shows highly single crystalline, large lateral dimensions (6−10 μm) and thin thickness (30−80 nm). Because of the absence of surface dangling bond on mica substrate, Te adatoms have a high migration rate along the mica surface

and thus promptly move toward growth sites, which results in a fast lateral growth of 2D Te hexagonal Te nanoplate without strict lattice match. The vdWE growth behavior of 2D hexagonal Te nanoplates on mica sheets are further evidenced by carrying out the growth experiments of Te nanostructures on Si substrate, where a large number of irregular microcrystals are observed even exerting the same experimental conditions as that on mica. Unique 2D geometry of regular Te hexagonal nanoplates facilitates their fabrications into functional electronic and optoelectronic device. In this work, we have fabricated single 2D Te hexagonal nanoplate photodetector directly on flexible mica growth substrate. High photoresponse is observed in two-terminal 2D Te hexagonal nanoplate device even after bending the flexible mica sheet for 100 times. While the focus of this work is on 2D Te hexagonal nanoplates, we believe that this understanding can be applied to exploit 2D nanostructures of other nonlayered materials such Se and Se/Te alloy which share the same crystal structure as that of Te. Furthermore, our work may pave the way toward utilizing 2D Te hexagonal nanoplates as the templates to generate a wealth of Te-based 2D functional nanomaterials such as ZnTe and CdTe by solution phase methods as the works done on Te nanowries.[31,32]

RESULTS AND DISCUSSION

Different from the previous vapor phase deposition of Te nanostructures,[21,28] fluorophlogopite mica [$KMg_3(AlSi_3O_{10})F_2$] sheets with exposed surface (001) were used as substrates. Fluorophlogopite mica sheets with pseudohexagonal Z_2O_5 (Z = Si, Al) layered structure were first mechanically cleaved into flexible transparent thin flakes (Figure 1(b)). More details of the growth process and characterization are described in the Materials and Methods section. The optical microscope (OM) images in Figure 1(c) are obtained from the synthesized products on flexible transparent thin flakes. The typical shape of Te nanostructures are regular 2D Te hexagonal nanoplates (Figure 1(c) inset) with lateral dimension of about 6−10 μm. The atomic force microscopy (AFM) was carried out to show the morphologies and thickness of 2D Te hexagonal nanoplates. As indicated by Figure 1(d), Figures S1 and S2 and Table S1 (Supporting Information), thickness of 2D Te hexagonal nanoplates mainly distributes in 30−80 nm. Interestingly, optical color image shows different colors of Te nanoplates with similar nanoplate lateral size. We have performed the AFM measurements of Te nanoplates with different optical colors. The results shows the optical colors are highly related to their thickness. As shown in Figure S2 (Supporting Information), the thickness of yellow Te nanoplate is ~38 nm. While for olive-green Te nanoplate, the thickness increases to ~86 nm. The optical colors of Te nanoplates gradually become dark with the increase of thickness. Optical contrast dependence of thickness provides a facile way to roughly identify the vertical dimensions of Te nanoplates.[36] Physical origin of large optical contrast is ascribed to strong amplitude modulation of absorption in the Te nanoplates. In addition, some 2D Te hexagonal nanoplates are found to be enclosed by a large number of Te nanoislands, which may result from the repeative nucleation of Te atoms at the edges of 2D Te nanoplates in the growth process. We will clearly explain this special morphology of Te nanoplates in the later analysis.

The transmission electron microscopy (TEM) was applied to reveal the microstructure and chemical composition of Te nanoplates. The synthesized Te nanoplates were released into the ethanol by sonication of flexible mica substrates about 24 h. Then the nanoplates were further dispersed onto copper grid for the TEM measurements. Figure 2(a) shows one complete Te nanoplate with hexagonal profile. Further characterization of high-resolution TEM (HRTEM) (Figure 2(b)) obtained from one corner of Te nanoplates clearly demonstrate the well-defined single crystalline of hexagonal Te nanoplates. As marked by two intersecting red lines, the HRTEM image exposes two sets of distinct lattice fringes with periodic space of 3.8 Å. The angle between two fringes is measured to be 120°, which is in agreement with the characteristic of hexagonal phase. The *in situ* selected area electron diffraction (SAED) as an inset in Figure 2(b) exhibits a set of perfect hexagonal pattern, indicating 2D Te nanoplates are of highly single-crystalline hexagonal phase. Furthermore, the hexagonally symmetric pattern manifests 2D Te hexagonal nanoplate is surrounded by (100), (1−10), (0−10), (−100), (−110) and (010) planes with top surface of (001). HRTEM image at the edge of Te nanoplate is shown in Figure 2(c) with inset of corresponding low-magnification TEM. Distinctive nanoparticles are found to be formed at the margin of Te nanoplates, which may be caused by repeated nucleation of Te atoms along the edges of Te nanoplate during the growth process. The nanoparticles observed at the margin of Te nanoplate in HRTEM images are consistent with the results of AFM images as shown in Figure 1(d), where abundant Te nanoislands are found at the edge of 2D Te hexagonal nanoplate. In order to obtain more information regarding the samples' composition and structure. The samples are further characterized by electron energy dispersive X-ray spectroscopy (EDX), Raman and Photoluminescence (PL). EDX study in Figure 2(d) proves the composition of synthesized products is elemental semiconductor Te. Peaks of Cu, Fe and Co results from copper grid. Raman scattering measurements in Figure 2(e) shows Te nanoplate has strong Raman-active phonon modes because of its high atomic number and large electronic polarizability. The strongest peak at 117.3 cm^{-1} is related to the A_1 model,

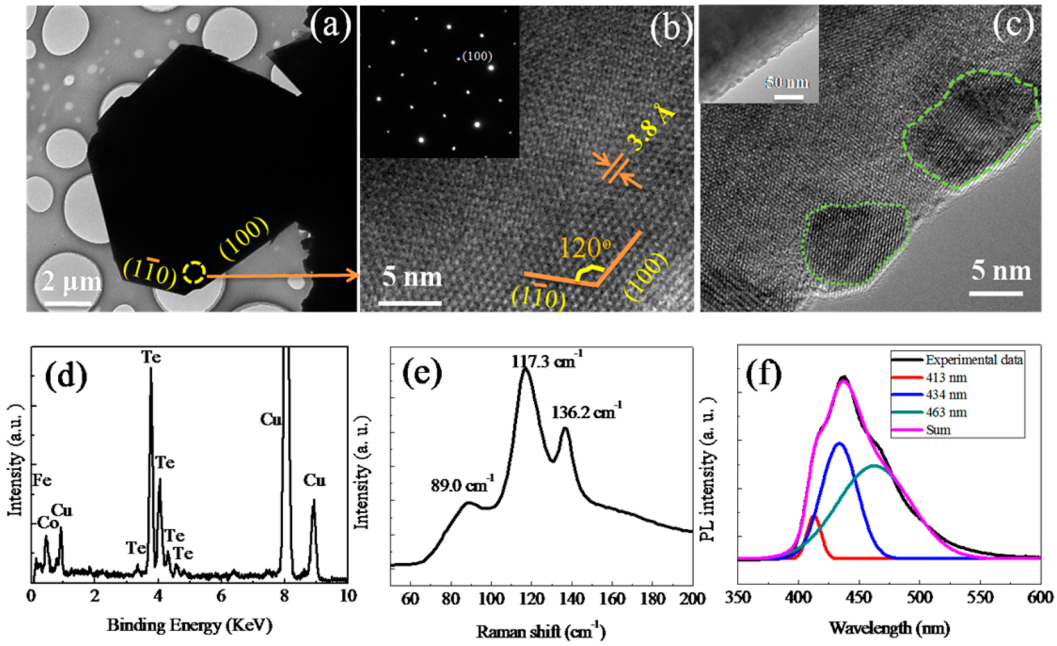

Figure 2. (a) Low-magnification TEM image of individual 2D Te hexagonal nanoplate. (b) Typical HRTEM image obtained from the corner of hexagonal Te nanoplate. Inset: corresponding SAED. (c) HRTEM image achieved on the edge of Te nanoplate, suggesting new nucleation at the sides of hexagonal Te nanoplate. Inset is the corresponding low-magnification TEM image. (d) EDX obtained from the same hexagonal Te nanoplate in (a). (e) Raman of a Te hexagonal nanoplate. (f) PL of Te hexagonal nanoplates excited by 325 nm laser (black line). The deconvolution of the band gives three Gaussian components with peaks at 413, 434, and 463 nm.

corresponding to the atoms moving in the basal plane.[37] Peaks at 89.0 and 136.2 cm^{-1} both belongs to degenerate E modes.[37] Peak of 89.0 cm^{-1} is caused by *a*- and *b*-axis rotation and peak of 136.2 cm^{-1} is related to asymmetric stretching mainly along the *c*-axis.[37] Figure 2(f) exhibits the PL of Te nanoplate excited at 325 nm. The deconvolution of the strong and broad peak produces three Gaussian components centered at 413, 434, and 463 nm. The PL characteristics in our work are in accordance with that of Te nanowires reported by S. Yu *et al.*[38] The PL of Te nanoplates primarily distributes over the range of 2.2−3.1 eV which is much larger than the band gap of Te (0.34 eV). According to the self-consistent Hartree−Fock−Slater calculation[39] and optical absorption spectrum[40] of Te, PL peak at 413 nm in our work should be electron radiation transition from p-antibonding triple of conduction band (CB) to p-bonding triple of valence band (VB). Peaks at 434 and 463 nm are likely the electron radiation transition from p-antibonding triple of CB to p-lone-pair triple of VB. Excellent PL behavior of Te hexagonal nanoplates hints their promising application in optoelectronic device.

Now we focus on the growth mechanism of 2D Te hexagonal nanoplate. As illustrated in Figure 3(a,b), two major steps are involved in the growth process that (1) growth of 3D Te nanoislands and (2) formation of 2D regular Te hexagonal nanoplate. At the initial stage, Te atoms first gather into individual Te nanoisland (Figure 3(c)). The substrate temperature and the growth duration of the initial stage is 500 °C and 20 min, respectively. And then Te nanoislands become

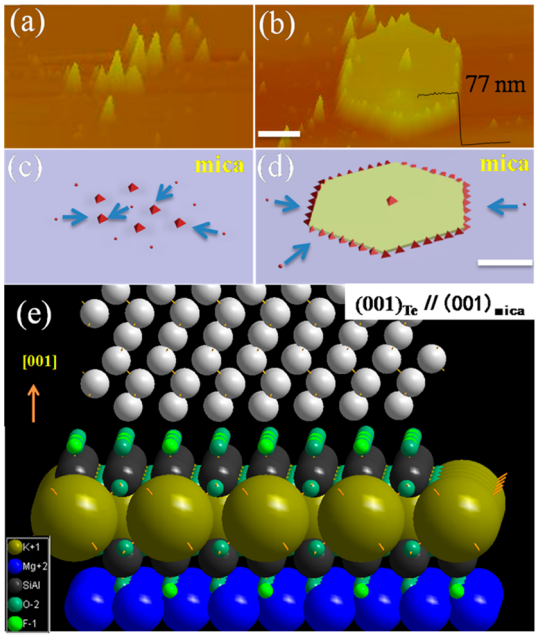

Figure 3. Schematic illuminations for the evolution process of 2D Te hexagonal nanoplate. (a) AFM images of Te nanoislands at the initial stage of growth process and (b) a complete 2D Te hexagonal nanoplate, scale bar in (b) is 2 μm. (c,d) The simulation for the growth process of Te nanostructure corresponding to (a) and (b), respectively. Scale bar in (d) is 2 μm. (e) Crystal structure model for the Te and mica at the interface. The bottom surface of Te nanplate (001)$_{Te}$ is parallel to the top surface of mica (001)$_{mica}$.

big and coalesce into a large Te nanoparticle (not shown in Figure 3). Thus, the growth of Te hexagonal nanoplate follows the Volmer−Weber (VW) model,

where 3D isolated islands are first formed and then merged into single structure.[41] With continuous supply of Te atoms, the single Te nanoparticle gradually grows into a perfect hexagonal Te nanoplate (Figure 3(d)). It is worth to note that in this stage new Te nanoislands are formed at the edges of Te hexagonal nanoplate due to the reduplicative nucleation of Te atoms as demonstrated in HRTEM of Figure 2(c). However, Te nanoplates displayed in Figures S1(b−d) and S2(b−e) (Supporting Information) do not show obvious nanoislands at the edge. Since Te nanoplate grows faster along lateral direction than vertical direction, lateral (100) equivalent planes should be more active than top (001) surface. That means lateral (100) equivalent planes are the growth active sites in the whole growth process. Te adatoms tend to diffuse toward these active sites and combine with Te atoms at the edge. As Te has a strong tendency to become one-dimensional structure, Te nanoislands with sharp tips are first formed at the edge of Te nanoplates. That is the reason why Te nanoislands occurs mainly at the edge of Te nanoplates and their thickness is larger than that of remaining body. However, that also means Te nanoislands should exist within the body with the growth of Te hexagonal nanoplate. Actually, the sharp tips of Te nanoislands are unstable. Te atoms on the sharp tips tend to diffuse toward lateral (100) planes, leaving the stable top (001) surface. As a result, there are no obvious nanoislands on the body and at the edge of most Te nanoplates. Te nanoplate shown in Figure S1(b) (Supporting Information) is a special case, where a large number of Te nanoislands are found on the top (001) surface as demonstrated in its three-dimensional AFM image of Figure S3 (Supporting Information). However, these Te nanoislands are much smaller than Te nanoislands at the edge, which further proves the sharp tips of Te nanoislands are unstable. With the growth of Te nanoplate, sharp tips will gradually decompose. Consequently, for Te nanoplates with nanoislands on the body and at the edge, the Te nanoislands will finally disappear if the reaction is sufficient. That is why we see most Te nanoplates as shown in Figures S1(b−d) and S2(b−e) (Supporting Information) do not show obvious nanoislands within the body and at the edge.

It is worth to note that the lateral dimension of hexagonal nanoplate increases with the increase of thickness. In order to accurately estimate the relationship between thickness and lateral dimension, we made a statistics on the distribution of lateral size as shown in Table S1 (Supporting Information). The average lateral dimension of Te hexagonal nanoplates with thickness of 30−60 nm is 4.5 μm. This value increases to 6.1 μm with increase of thickness from 30−60 nm to 70−90 nm. Further increase the thickness to 90−120 nm, the lateral size reaches up to 8.9 μm. Consequently, the lateral dimension significantly increases with the increase of hexagonal nanoplate thickness. Obviously, the growth rate along lateral direction (G_l) is much faster than that along vertical direction (G_v), leading to the lamellar 2D Te nanoplate.

The mica substrate used in this work is crucial for the formation of Te hexagonal nanoplates. In this work, the mica sheets are mechanically cleaved along (001) surface, which is chemically inert due to the absence of surface dangling atoms as shown in Figure 3(e) (down). On the one hand, the chemically inert mica surface enable epitaxial growth of Te nanoplate along the lateral direction without strict lattice matching. On the other hand, weak van der Waals interaction between mica substrate and Te adatoms facilitates the lateral migration of Te adatoms on mica surface, and thus accelerating the growth of Te nanoplate along the lateral direction. The vdWE effect of Te hexagonal nanoplate on mica is definitely confirmed by the growth of Te microcrystals on Si. Under the same reaction conditions as that for Te hexagonal nanoplate on mica, a layer of Te microcrystals with various morphologies are obtained (Figure S4, Supporting Information). In contrast to mica surface, three-dimensionally bonded Si has dangling bond at the surface. The strong chemical bonding interaction between Si surface and Te overlayer significantly increases the migration barrier energy of Te adatoms along the Si surface. In this case, Te adatoms are expected to accumulate toward vertical direction. In addition, irregular shapes of Te microcrystals are likely caused by the large lattice mismatch at the interface between Te overlayer and Si substrate, which prevents the incommensurate epitaxy of Te microcrystals. Except for the chemically inert surface provided by mica, substrate temperature is also important for the growth of planar Te nanoplates with special exposed surface. We believe, under the growth temperature of 500 °C in our work, (100) equivalent planes of Te nanoplates are likely more active than the top (001) surface. Normally, during the nucleation and the growth, the vapor atoms prefer to fuse with the high energy crystallographic planes in the crystal lattice system.[42] Thus, the high active (100) equivalent planes of Te nanoplates grows faster than low active top (001) surface.

One thing should be noted that, unlike layered materials which prefer to become 2D nanoarchitectures due to its strong in-plane covalent bonding in individual atomic layers and weak van der Waals interaction between two adjacent layers, Te is more difficult to be grown into 2D nanostructures due to its helical chain-like structure.[22,25] Take topological insulator Bi_2Te_3 as an example,[2,7] Bi_2Te_3 has a layered structure where Bi and Te atoms bind covalently in each planar quintuple layer (QL). The QLs hold together by weak van der Waals interaction. In the growth process of Bi_2Te_3 nanoplates, the incoming atoms tend to find the dangling bonds at the edge of the nuclei and bind covalently with atoms at the edge. Although some atoms are first adsorbed on the top (001) surface,

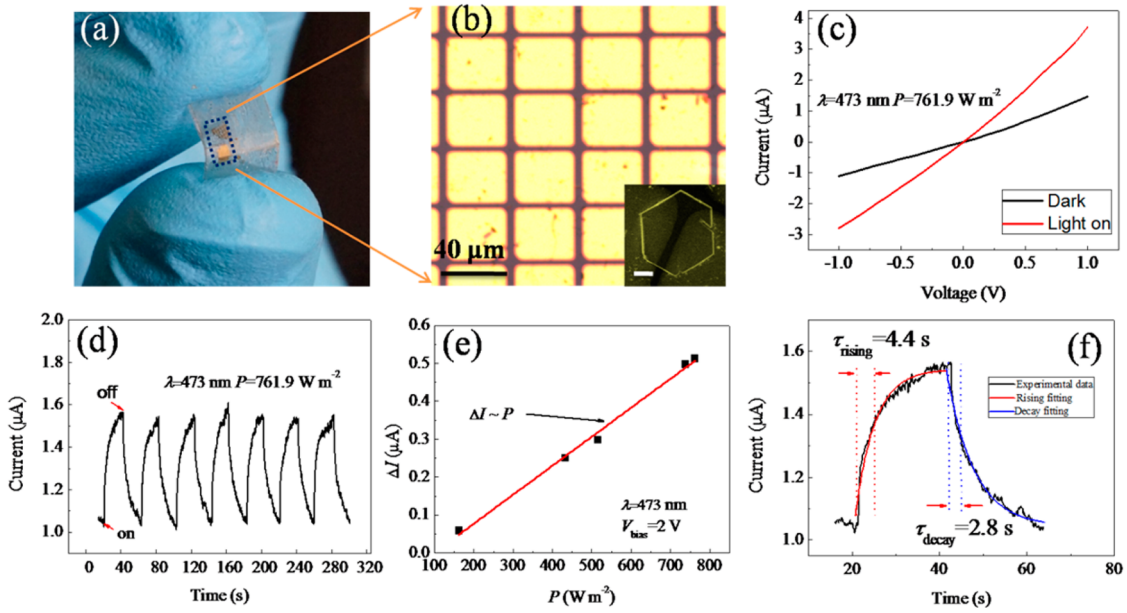

Figure 4. (a) Photograph of 2D Te hexagonal nanoplates-based device. (b) OM image of electrodes pattern. Inset: single Te hexagonal nanoplate photodetector, scale bar = 2 μm. (c) $I-V$ curves in the dark and in the presence of 473 nm laser of single Te hexagonal nanoplate photodetector. (d) Time-dependent photoresponse of Te hexagonal nanoplate device with voltage bias of 2 V. (e) Power dependence of photocurrent at 2 V bias. (f) A separated response and reset cycle.

they quickly diffuse toward the edges since top (001) surface is passivated by chemically saturated Te atoms. Consequently, Bi_2Te_3 can be easily grown into 2D ultrathin nanoplates with lateral size of several micrometers and vertical thickness of a few QLs even on the oxidized silicon.[2] With further utilization of chemically inert mica sheets, the lateral dimension of Bi_2Te_3 triangle nanoplates reaches up to 0.1 mm. In addition, the orientation of Bi_2Te_3 triangle nanoplates can even be controlled to the multiples of ~60°. The growth positions can also be adjusted by using selective oxygen plasma etching.[7] In contrast to Bi_2Te_3, Te has a helical chain-like crystal structure as presented in Figure 1(a). Te atoms first form the helical chains along *c*-axis by the covalent bonding. Then helical chains can be readily packed into one-dimensional hexagonal crystal structure through van der Waals interactions. However, with the help of chemically inert mica sheets, the growth of Te nanoplate along the lateral direction becomes much faster since (1) the chemically inert mica surface enable epitaxial growth of Te nanoplate along the lateral direction without strict lattice matching and (2) weak van der Waals interaction between mica substrate and Te adatoms facilitates the lateral migration of Te adatoms on mica surface, thus accelerating the growth of Te nanoplate along the lateral direction. However, the vertical size of Te nanoplate also slowly increases with the increase of lateral dimension as demonstrated in Table S1 (Supporting Information) since Te adatoms can be bonded by the unsaturated Te atoms on top (001) surface *via* covalent interaction. As a result, the thickness of Te nanoplate (~30−80 nm) obtained in our work is much larger than that of Bi_2Te_3 triangle nanoplates (a few QLs). The larger and thinner Te nanoplates may be obtained by further increasing the activation of lateral (100) equivalent planes and reducing the activation of top (001) surface *via* modulating the substrate temperature. The successful realization of 2D Te hexagonal nanoplates in this work may pave the way toward leveraging vdWE as a useful channel to synthesize 2D nanostructure of other nonlayered materials.

Unique planar structure of 2D Te hexagonal nanoplate on flexible mica sheets enables the fabrication of functional electronic and optoelectronic device. In this work, we *in situ* construct a photodetector based on 2D Te hexagonal nanoplate on flexible mica sheets as indicated in Figure 4(a,b). Figure 4(c) shows the current (I)-voltage (V) characteristics of a Te hexagonal nanoplate device in the dark and in the presence of laser with wavelength of 473 nm and light intensity of 761.9 W m^{-2}. A pronounced photoconducting response is observed when the device is irradiated by 473 nm laser. To study the stability of the device, time dependence of photoresponse was performed at room temperature as shown in Figure 4(d). With the illumination on and off, the current exhibits the same level of both noise and photocurrent, suggesting high stability and repeatability of our device. Here, photocurrent (ΔI) is defined by the difference between I_{on} and I_{off}. The large dark current may be caused by vacancies and surface defects of Te hexagonal nanoplate. In addition, linear relationship (Figure 4(e)) between ΔI and laser intensity within the range of 161.9−761.9 W m^{-2} fully reflects that Te hexagonal nanoplate device should be a typical photon-dependent resistor that means more

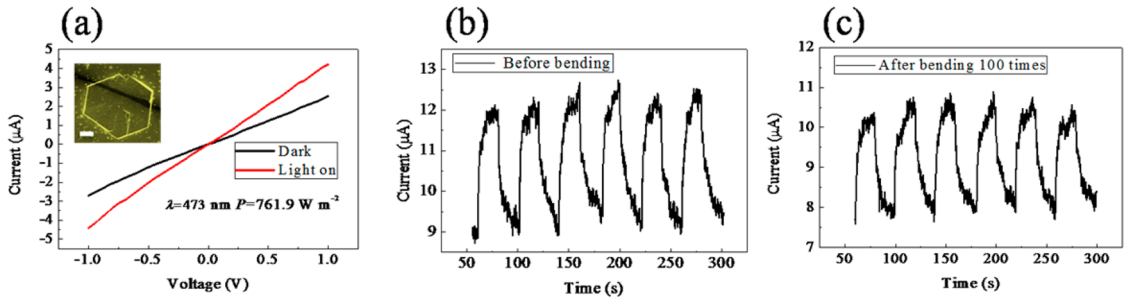

Figure 5. (a) *I*−*V* curves in the dark and in the presence of 473 nm laser of another Te hexagonal nanoplate photodetector. Inset: SEM image of the device with scale bar of 1 μm. Time trace of photoresponse when laser was toggled on and off before (b) and after bending the device for 100 times (c).

photons produces more carriers. Exponential functions were used to fit the rising and decaying curve of an enlarged single cycle as shown in Figure 4(f), indicating that the response time (τ_{rising}) and recovery time (τ_{decay}) are 4.4 and 2.8 s, respectively. Here, τ_{rising} is related to the time taken from the dark current increasing to $1-1/e \approx 63\%$ of the maximum photocurrent, and the τ_{decay} is taken from the $1/e \approx 37\%$ of the maximum photocurrent.[43] Both of the rising time and recovery time of Te nanoplages are larger than that of few-layer GaSe nanoplates[3] and single-layer MoS_2.[44] Generally speaking, the absorption and desorption of gas molecules on the surface are an important factors that affects the rise and decay times.[43] Take the ZnO nanosensor as an example, the oxygen absorption and desorption on the surface of ZnO nanowires caused the slow UV response and recovery.[45] After surface passivation, the rising and decay time both decrease from about one second to a few milliseconds. The surface functionalization significantly reduce the number of active sites on the surface of ZnO nanowires and thus eliminate the impact of oxygen absorption and desorption. As to the Te nanoplate, gas molecules may influence its photoresponse if surface of Te nanoplates resides a large amount of active sites. However, the trap states inside the material can also severely deteriorate the rise and decay speed.[46] Te nanoplates obtained in our work may be the imperfect semiconductor and have large number of trap states. Thus, photogenerated carriers first fill the trap states and then reach the maximum when Te nanoplates are illuminated, which prolongs the response time. Consequently, once the light is turned off, partial carriers will be released slowly from the trap centers, which deteriorates the reset speed.[46] From this point, the thickness of Te nanoplates has a strong effect on τ_{rising} and τ_{decay} since the thicker Te nanoplate have more trap states inside the material than that of GaSe nanoplate[3] and single layer MoS_2.[44]

In situ fabrication of Te hexagonal nanoplate photodetector on mica sheets make the device possesses highly flexible. Figure 5(a) displays the photoresponse of another Te hexagonal nanoplate photodetector on flexible mica sheets as shown in Figure 4(a). The drastic increase in current under 473 nm laser illumination is observed compared with the current in the dark. In order to investigate the durability of the flexible photodetector based on 2D Te hexagonal nanoplates, the photoresponse of the devices fabricated on flexible mica sheets was measured before and after repeatedly bending the device. Figure 5(b) and (c) plots the photoresponse *versus* time with the 473 nm laser on and off before and after continuously bending the device for 100 times, respectively. Noise current reduces from ~9.3 to ~7.9 μA and photocurrent decreases from ~2.7 to ~2.3 μA. A slight decrease of both noise current and photocurrent may be caused by the higher contact barrier due to the relaxation of the electrode contacts after bending the device for 100 times. High stability of 2D hexagonal Te nanoplate-based photodetector on flexible mica sheets may open up their applications opportunity in flexible and wearable device. It worth to note that 2D hexagonal Te nanoplate-based photodetector shows very large photoresponsivity (R_λ). Here, R_λ is defined as the photocurrent generated per unit power of incident light on the effective area of a photodetector. R_λ of devices used in Figure 4 and Figure 5 are measured to be 162.4 and 389.5 A/W respectively. The high photoresponsivity of Te hexagonal nanoplate on flexible mica sheets indicates its promising application in functional optoelectronic device. Here, the illuminated area of devices used in Figure 4 and Figure 5 is 24.0 μm^2 and 10.0 μm^2, respectively. Both of the devices are measured under the voltage bias of 2 V.

CONCLUSION

In summary, we succeeded in vdWE growth of 2D Te hexagonal nanoplate by using mica substrate. The thickness and lateral dimension of 2D Te hexagonal nanoplate can be controlled to 30−80 nm and 6−10 μm, respectively. Although Te has a strong tendency to become 1D nanoarchitecture due to its highly anisotropic crystal structure, the Te nanoislands are still developed into regular 2D Te hexagonal nanoplate since mica sheets greatly increase the lateral growth rate of 2D Te hexagonal nanoplate. Because of the absence of surface dangling bonds, mica supply

a ideal vdWE substrates, which profoundly enhances the large migration rate of Te adatoms along mica surface. This function can be further evidenced by using Si as the growth substrates, where a layer of irregular Te microcrystals are obtained although exerting the same experimental conditions as that on mica sheet. Unique 2D geometry of Te hexagonal nanoplate facilitates the fabrication of functional electronic and optoelectronic device. In this work, Te hexagonal nanoplates-based photodetector is *in situ* fabricatied on flexible mica sheets. High photoresponse is observed even after bending the device for 100 times, indicating the device has a great application potential in flexible and wearable optoelectronic device. As a case of study, our work may lead to the widely exploitation of vdWE on the controlled synthesis of 2D nanostructure of other nonlayered functional materials such as Se and Se/Te alloy, which share the same crystal structure as that of tellurium.

MATERIALS AND METHODS

Synthesis of 2D Hexagonal Te Nanoplates. 2D hexagonal Te nanoplates were obtained by using PVD method in horizontal vacuum tube furnace with single temperature zone. Te powder was loaded (99.99%, alfa aesar) in the center of quartz tube. Fluorophlogopite mica [$KMg_3(AlSi_3O_{10})F_2$] sheets or Si wafer were placed in the downstream area. The sealed quartz tube was evacuated and flushed few times with high purity Ar gas in order to provide oxygen free environment. In the growth process, Ar gas was fed with a constant flow rate of 100 sccm by maintaining tube pressure of 100 mbar. The whole reaction process was carried out under the furnace temperature of 750 °C for the source and 500 °C for the substrate. The reaction process was maintained for 60 min. And then the furnace was naturally cooled down to the room temperature.

Characterizations. Morphology, composition and microstructure of the synthesized products were characterized by optical microscope (OM, Olympus BX51M), field emission scanning electron microscopy (FESEM, Hitach S4800), atomic force microscopy (AFM, Veeco Multimode), Raman (Renishaw InVia, 532 nm excitation laser), transmission electron microscopy (TEM) and high-resolution transmission electron microscope (HRTEM), selected area electron diffraction (SAED) and electron energy dispersive X-ray spectroscopy (EDX) attached to the TEM. Photoluminescence (PL) were collected by using a 325 nm He−Cd laser (Kimmon, ik3301R-G) to excite the samples. The PL signals was dispersed by a 550 mm spectrometer (HORIBA JobinYvon) and detected by a Si-CCD cooled by liquid nitrogen.

Fabrication and Measurements of 2D Te Hexagonal Nanoplate-Based Photodetector. Two-terminal electrodes of individual Te nanoplate were *in situ* fabricated. Copper grid shadow mask with typical gaps of 2 μm was covered on the surface of flexible mica sheet. Subsequently 8 nm Cr and 100 nm Au was evaporated, respectively. The electrical transport and photoresponse behavior of individual device were measured at room temperature in the ambient air using a manual probe station (Everbeing, BD4) equipped with a Keithley 4200 semiconductor characterization system. A 473 nm laser is employed to perform photoresponse experiments.

Conflict of Interest: The authors declare no competing financial interest.

Acknowledgment. This work at National Center for Nanoscience and Technology was supported by 973 Program of the Ministry of Science and Technology of China (No. 2012CB934103), the 100-Talents Program of the Chinese Academy of Sciences (No. Y1172911ZX), the National Natural Science Foundation of China (No. 21373065) and Beijing Natural Science Foundation (No. 2144059).

Supporting Information Available: OM and AFM images of 2D Te hexagonal nanoplates, SEM image of Te microcrystals grown on Si with same experimental condition on mica, thickness and lateral dimension distribution, growth comparison between Te hexagonal nanoplates and 2D layered materials, elucidation of the slow photoresponse speed of Te nanoplates. This material is available free of charge *via* the Internet at http://pubs.acs.org.

REFERENCES AND NOTES

1. Ji, Q.; Zhang, Y.; Gao, T.; Zhang, Y.; Ma, D.; Liu, M.; Chen, Y.; Qiao, X.; Tan, P.-H.; Kan, M. Epitaxial Monolayer MoS_2 on Mica with Novel Photoluminescence. *Nano Lett.* **2013**, *13*, 3870–3877.
2. Kong, D.; Dang, W.; Cha, J. J.; Li, H.; Meister, S.; Peng, H.; Liu, Z.; Cui, Y. Few-Layer Nanoplates of Bi_2Se_3 and Bi_2Te_3 with Highly Tunable Chemical Potential. *Nano Lett.* **2010**, *10*, 2245–2250.
3. Zhou, Y.; Nie, Y.; Liu, Y.; Yan, K.; Hong, J.; Jin, C.; Zhou, Y.; Yin, J.; Liu, Z.; Peng, H. Epitaxy and Photoresponse of Two-Dimensional GaSe Crystals on Flexible Transparent Mica Sheets. *ACS Nano* **2014**, *8*, 1485–1490.
4. Hong, Y. J.; Yang, J. W.; Lee, W. H.; Ruoff, R. S.; Kim, K. S.; Fukui, T. Van der Waals Epitaxial Double Heterostructure: InAs/Single-Layer Graphene/InAs. *Adv. Mater.* **2013**, *25*, 6847–6853.
5. Zhang, X.; Meng, F.; Christianson, J. R.; Arroyo-Torres, C.; Lukowski, M. A.; Liang, D.; Schmidt, J. R.; Jin, S. Vertical Heterostructures of Layered Metal Chalcogenides by van der Waals Epitaxy. *Nano Lett.* **2014**, *14*, 3047–3054.
6. Zhu, Y.; Zhou, Y.; Utama, M. I. B.; de la Mata, M.; Zhao, Y. Y.; Zhang, Q.; Peng, B.; Magen, C.; Arbiol, J.; Xiong, Q. H. Solution Phase van der Waals Epitaxy of ZnO Wire Arrays. *Nanoscale* **2013**, *5*, 7242–7249.
7. Li, H.; Cao, J.; Zheng, W.; Chen, Y.; Wu, D.; Dang, W.; Wang, K.; Peng, H.; Liu, Z. Controlled Synthesis of Topological Insulator Nanoplate Arrays on Mica. *J. Am. Chem. Soc.* **2012**, *134*, 6132–6135.
8. Utama, M. I. B.; Zhang, Q.; Zhang, J.; Yuan, Y.; Belarre, F. J.; Arbiol, J.; Xiong, Q. Recent Developments and Future Directions in the Growth of Nanostructures by van der Waals Epitaxy. *Nanoscale* **2013**, *5*, 3570–3588.
9. Garcia, J. M.; Wurstbauer, U.; Levy, A.; Pfeiffer, L. N.; Pinczuk, A.; Plaut, A. S.; Wang, L.; Dean, C. R.; Buizza, R.; Van Der Zande, A. M. Graphene Growth on h-BN by Molecular Beam Epitaxy. *Solid State Commun.* **2012**, *152*, 975–978.
10. Lippert, G.; Dabrowski, J.; Lemme, M.; Marcus, C.; Seifarth, O.; Lupina, G. Direct Graphene Growth on Insulator. *Phys. Status Solidi B* **2011**, *248*, 2619–2622.
11. Min, L.; Di, W.; Yu, Z.; Wei, H.; Wei, J.; Wenshan, Z.; Shuli, Z.; Chuanhon, J.; Guo, Y.; Peng, H.; Liu, Z. Controlled Growth of Atomically Thin In_2Se_3 Flakes by van der Waals Epitaxy. *J. Am. Chem. Soc.* **2013**, *135*, 13274–13277.
12. Shi, Y.; Zhou, W.; Lu, A.-Y.; Fang, W.; Lee, Y.-H.; Hsu, A. L.; Kim, S. M.; Kim, K. K.; Yang, H. Y.; Li, L.-J. Van der Waals Epitaxy of MoS_2 Layers using Graphene as Growth Templates. *Nano Lett.* **2012**, *12*, 2784–2791.
13. Xu, K.; Wang, Z.; Du, X.; Safdar, M.; Jiang, C.; He, J. Atomic-Layer Triangular WSe_2 Sheets: Synthesis and Layer-Dependent Photoluminescence Property. *Nanotechnology* **2013**, *24*, 465705.
14. Wisotzki, E.; Klein, A.; Jaegermann, W. Van der Waals' Condensation of ZnSe on Layered GaSe van der Waals' Surfaces: A New Route to Self-Organized Well-Defined Quantum Dot Structures. *Adv. Mater.* **2005**, *17*, 1173–1177.

15. Kim, Y.-J.; Lee, J.-H.; Yi, G.-C. Vertically Aligned ZnO Nanostructures Grown on Graphene Layers. *Appl. Phys. Lett.* **2009**, *95*, 213101.
16. Hong, Y. J.; Lee, W. H.; Wu, Y.; Ruoff, R. S.; Fukui, T. Van der Waals Epitaxy of InAs Nanowires Vertically Aligned on Single-Layer Graphene. *Nano Lett.* **2012**, *12*, 1431–1436.
17. Munshi, A. M.; Dheeraj, D. L.; Fauske, V. T.; Kim, D.-C.; van Helvoort, A. T.; Fimland, B.-O.; Weman, H. Vertically Aligned GaAs Nanowires on Graphite and Few-Layer Graphene: Generic Model and Epitaxial Growth. *Nano Lett.* **2012**, *12*, 4570–4576.
18. Utama, M. I. B.; Belarre, F. J.; Magen, C.; Peng, B.; Arbiol, J.; Xiong, Q. Incommensurate van der Waals Epitaxy of Nanowire Arrays: A Case Study with ZnO on Muscovite Mica Substrates. *Nano Lett.* **2012**, *12*, 2146–2152.
19. Utama, M. I. B.; Zhang, Q.; Jia, S.; Li, D.; Wang, J.; Xiong, Q. Epitaxial II-VI Tripod Nanocrystals: A Generalization of van der Waals Epitaxy for Nonplanar Polytypic Nanoarchitectures. *ACS Nano* **2012**, *6*, 2281–2288.
20. Liu, P.; Ma, Y.; Cai, W.; Wang, Z.; Wang, J.; Qi, L.; Chen, D. Photoconductivity of Single-Crystalline Selenium Nanotubes. *Nanotechnology* **2007**, *18*, 205704.
21. Safdar, M.; Zhan, X.; Niu, M.; Mirza, M.; Zhao, Q.; Wang, Z.; Zhang, J.; Sun, L.; He, J. Site-Specific Nucleation and Controlled Growth of a Vertical Tellurium Nanowire Array for High Performance Field Emitters. *Nanotechnology* **2013**, *24*, 185705.
22. Xia, Y.; Yang, P.; Sun, Y.; Wu, Y.; Mayers, B.; Gates, B.; Yin, Y.; Kim, F.; Yan, H. One-Dimensional Nanostructures: Synthesis, Characterization, and Applications. *Adv. Mater.* **2003**, *15*, 353–389.
23. Cao, X.; Xie, Y.; Li, L. Spontaneous Organization of Three—Dimensionally Packed Trigonal Selenium Microspheres into Large-Area Nanowire Networks. *Adv. Mater.* **2003**, *15*, 1914–1918.
24. Gates, B.; Mayers, B.; Cattle, B.; Xia, Y. Synthesis and Characterization of Uniform Nanowires of Trigonal Selenium. *Adv. Funct. Mater.* **2002**, *12*, 219.
25. Wang, Q.; Safdar, M.; Wang, Z.; He, J. Low-Dimensional Te-Based Nanostructures. *Adv. Mater.* **2013**, *25*, 3915–3921.
26. Wang, Q.; Safdar, M.; Zhan, X.; He, J. Controllable Wettability by Tailoring One-Dimensional Tellurium Micro−Nanostructures. *CrystEngComm* **2013**, *15*, 8475–8482.
27. Zhu, Y. J.; Wang, W. W.; Qi, R. J.; Hu, X. L. Microwave-Assisted Synthesis of Single-Crystalline Tellurium Nanorods and Nanowires in Ionic Liquids. *Angew. Chem.* **2004**, *116*, 1434–1438.
28. Hawley, C. J.; Beatty, B. R.; Chen, G.; Spanier, J. E. Shape-Controlled Vapor-Transport Growth of Tellurium Nanowires. *Cryst. Growth Des.* **2012**, *12*, 2789–2793.
29. Gates, B.; Yin, Y.; Xia, Y. A Solution-Phase Approach to the Synthesis of Uniform Nanowires of Crystalline Selenium with Lateral Dimensions in the Range of 10−30 nm. *J. Am. Chem. Soc.* **2000**, *122*, 12582–12583.
30. Jiang, X.; Mayers, B.; Herricks, T.; Xia, Y. Direct Synthesis of Se@CdSe Nanocables and CdSe Nanotubes by Reacting Cadmium Salts with Se Nanowires. *Adv. Mater.* **2003**, *15*, 1740–1743.
31. Tai, G.; Zhou, B.; Guo, W. Structural Characterization and Thermoelectric Transport Properties of Uniform Single-Crystalline Lead Telluride Nanowires. *J. Phys. Chem. C* **2008**, *112*, 11314–11318.
32. Wang, K.; Liang, H.-W.; Yao, W.-T.; Yu, S.-H. Templating Synthesis of Uniform Bi_2Te_3 Nanowires with High Aspect Ratio in Triethylene Glycol (TEG) and Their Thermoelectric Performance. *J. Mater. Chem.* **2011**, *21*, 15057–15062.
33. Zhang, G.; Fang, H.; Yang, H.; Jauregui, L. A.; Chen, Y. P.; Wu, Y. Design Principle of Telluride-Based Nanowire Heterostructures for Potential Thermoelectric Applications. *Nano Lett.* **2012**, *12*, 3627–3633.
34. Safdar, M.; Wang, Z.; Mirza, M.; Butt, F. K.; Wang, Y.; Sun, L.; He, J. Telluride-Based Nanorods and Nanosheets: Synthesis, Evolution and Properties. *J. Mater. Chem. A* **2013**, *1*, 1427–1432.
35. Huang, L.; Yu, Y.; Li, C.; Cao, L. Substrate Mediation in Vapor Deposition Growth of Layered Chalcogenide Nanoplates: A Case Study of $SnSe_2$. *J. Phys. Chem. C* **2013**, *117*, 6469–6475.
36. Kong, D. S.; Dang, W. H.; Cha, J. J.; Li, H.; Meister, S.; Peng, H. L.; Liu, Z. F.; Cui, Y. Few-Layer Nanoplates of Bi_2Se_3 and Bi_2Te_3 with Highly Tunable Chemical Potential. *Nano Lett.* **2010**, *10*, 2245–2250.
37. Martin, R. M.; Lucovsky, G.; Helliwell, K. Intermolecular Bonding and Lattice Dynamics of Se and Te. *Phys. Rev. B: Solid State* **1976**, *13*, 1383.
38. Qian, H.-S.; Yu, S.-H.; Gong, J.-Y.; Luo, L.-B.; Fei, L.-f. High-Quality Luminescent Tellurium Nanowires of Several Nanometers in Diameter and High Aspect Ratio Synthesized by A Poly(vinyl pyrrolidone)-Assisted Hydrothermal Process. *Langmuir* **2006**, *22*, 3830–3835.
39. Isomaki, H. M.; Boehm, J. v. Optical Absorption of Tellurium. *Phys. Scr.* **1982**, *25*, 801–803.
40. Lin, Z.-H.; Yang, Z.; Chang, H.-T. Preparation of Fluorescent Tellurium Nanowires at Room Temperature. *Cryst. Growth Des.* **2008**, *8*, 351–357.
41. Ratsch, C.; Venables, J. Nucleation Theory and the Early Stages of Thin Film Growth. *J. Vac. Sci. Technol., A* **2003**, *21*, S96–S109.
42. Yan, Y. G.; Zhou, L. X.; Zhang, Y.; Zhang, J.; Hu, S. Q. Large-Scale Synthesis of In_2O_3 Nanocubes under Nondynamic Equilibrium Model. *Cryst. Growth Des.* **2008**, *8*, 3285–3289.
43. Cao, J.; Wang, Z.; Zhan, X.; Wang, Q.; Safdar, M.; Wang, Y.; He, J. Vertical SnSe Nanorod Arrays: from Controlled Synthesis and Growth Mechanism to Thermistor and Photoresistor. *Nanotechnology* **2014**, *25*, 105705.
44. Yin, Z.; Li, H.; Li, H.; Jiang, L.; Shi, Y.; Sun, Y.; Lu, G.; Zhang, Q.; Chen, X.; Zhang, H. Single-Layer MoS_2 Phototransistors. *ACS Nano* **2012**, *6*, 74–80.
45. Zhou, J.; Gu, Y.; Hu, Y.; Mai, W.; Yeh, P.-H.; Bao, G.; Sood, A. K.; Polla, D. L.; Wang, Z. L. Gigantic Enhancement in Response and Reset Time of ZnO UV Nanosensor by Utilizing Schottky Contact and Surface Functionalization. *Appl. Phys. Lett.* **2009**, *94*, 191103.
46. Jiang, Y.; Zhang, W. J.; Jie, J. S.; Meng, X. M.; Fan, X.; Lee, S. T. Photoresponse Properties of CdSe Single-Nanoribbon Photodetectors. *Adv. Funct. Mater.* **2007**, *17*, 1795–1800.